

Effects of Te- and Fe-doping on the superconducting properties in Fe_{1-x}Te thin films

Yalin Zhang

Nanjing University

Tong Wang

Nanjing University of Aeronautics and Astronautics

Zhihe Wang (✉ zhwang@nju.edu.cn)

Nanjing University

Zhongwen Xing

Nanjing University

Research Article

Keywords: feyse1, xtex, films, composition, thin, chemical

Posted Date: August 30th, 2021

DOI: <https://doi.org/10.21203/rs.3.rs-847481/v1>

License:  This work is licensed under a Creative Commons Attribution 4.0 International License.

[Read Full License](#)

Effects of Te- and Fe-doping on the superconducting properties in $\text{Fe}_y\text{Se}_{1-x}\text{Te}_x$ thin films

Yalin Zhang^{1,2}, Tong Wang³, Zhihe Wang^{1,4*}, and Zhongwen Xing^{1,5*}

¹National Laboratory of Solid State Microstructures and Collaborative Innovation Center of Advanced Microstructures, Nanjing University, Nanjing 210093, China

²College of Engineering and Applied Sciences, Nanjing University, Nanjing 210093, China

³Department of Mathematics, Nanjing University of Aeronautics and Astronautics, Nanjing 210016, China

⁴School of Physics, Nanjing University, Nanjing 210093, China

⁵School of Electronic Science and Engineering, Nanjing University, Nanjing 210093, China

Abstract

High quality $\text{Fe}_y\text{Se}_{1-x}\text{Te}_x$ epitaxial thin films have been fabricated on TiO_2 -buffered SrTiO_3 substrates by pulsed laser deposition technology. There is a significant composition deviation between the nominal target and the thin film. Te doping can affect the Se/Te ratio and Fe content in chemical composition. The superconducting transition temperature T_c is closely related to the chemical composition. Fe vacancies are beneficial for the $\text{Fe}_y\text{Se}_{1-x}\text{Te}_x$ films to exhibit the higher T_c . A 3D phase diagram is given that the optimize range is $x = 0.13 - 0.15$ and $y = 0.73 - 0.78$ for $\text{Fe}_y\text{Se}_{1-x}\text{Te}_x$ films. The anisotropic, effective pinning energy and critical current density for the $\text{Fe}_{0.72}\text{Se}_{0.94}\text{Te}_{0.06}$, $\text{Fe}_{0.76}\text{Se}_{0.87}\text{Te}_{0.13}$ and $\text{Fe}_{0.91}\text{Se}_{0.77}\text{Te}_{0.23}$ samples were studied in detail. The scanning transmission electron microscopy images display a regular pattern without obviously scale defects at the interfacial structure.

*Corresponding authors: zhwang@nju.edu.cn (Z.H. Wang); zwxing@nju.edu.cn (Z.W. Xing).

In 2008, Hosono *et al.* [1] first discovered the iron-based superconductor $\text{LaO}_{1-x}\text{F}_x\text{FeAs}$, which has a superconducting critical temperature of 26 K. Subsequently, Hsu *et al.* [2] reported that the binary superconductor FeSe with antiferromagnetic planes and has the transition temperature of 8 K. Through the applied pressure on the samples, the transition temperature can reach ~ 37 K [3, 4]. Xue *et al.* [5] reported a superconducting transition temperature above 100 K in single-layer FeSe film grown on a doped SrTiO_3 (STO) substrate by molecular beam epitaxy method. Due to its simple crystal structure, this binary FeSe system with higher T_c are available has attracted tremendous interest in exploring the mechanism of high-temperature superconductivity [6-8]. Generally, the FeSe layer is responsible for the superconductivity and the paired electrons are mainly 3d electrons of Fe ions. Meanwhile, the FeSe layers exhibit electrical neutrality and the atoms between the layers are bonded together by van der Waals [9, 10]. However, the same structure as FeTe does not show superconducting behavior. Yeh *et al.* [11] found that the Te atoms are replaced by partially substituted Se atoms, the antiferromagnetic can be suppressed and superconductivity is induced with a superconducting transition temperature of 15 K. In bulk crystals, the optimal Te content to achieve the highest T_c is considered to be $x \approx 0.6$, and phase separation occurs in the region of $0.1 \leq x \leq 0.3$ [12]. Liu *et al.* [13] have studied the electronic and magnetic phase diagram of $\text{Fe}_{1.02}\text{Se}_x\text{Te}_{1-x}$ single crystal superconductors. They showed that the phase diagram contains three regions, namely long-range antiferromagnetic order with a wave vector $(\pi, 0)$ in region I ($0 \leq x < 0.09$), neither long-range antiferromagnetic order nor bulk superconductivity in Region II ($0.09 < x < 0.29$) and the evidence of bulk superconductivity with the T_c about 14.5 K in Region III ($x \geq 0.29$). The phase diagram of $\text{FeSe}_{1-x}\text{Te}_x$ films on CaF_2 substrates showed that the maximum value of T_c is as high as 23 K at $x = 0.2$, and a sudden suppression of T_c is observed at $0.1 < x < 0.2$, whereas T_c increases with decreasing x for $0.2 \leq x < 1$ [14]. The interface effect between film and substrate makes it possible to obtain the $\text{Fe}_y\text{Se}_{1-x}\text{Te}_x$ films with high transition temperature in a metastable phase. Although researchers have reported many studies on superconducting mechanism of Fe(Se, Te) films that prepared by pulsed laser deposition (PLD), the bidirectional effect of chemical composition on the superconductivity of

$\text{Fe}_y\text{Se}_{1-x}\text{Te}_x$ films is uncertain [15-19]. In this paper, we have prepared different polycrystalline targets to grow $\text{Fe}_y\text{Se}_{1-x}\text{Te}_x$ films and did a detailed investigation on the superconducting properties and its phase diagram. The experimental results show that there is a significant deviation between the nominal compositions of polycrystalline targets and the real compositions of films. The increase of Te doping can have an impact not only on Se/Te ratio but also Fe content. The electrical transport results indicate that the optimal range of Te and Fe content is $x = 0.13 - 0.15$ and $y = 0.73 - 0.78$ for $\text{Fe}_y\text{Se}_{1-x}\text{Te}_x$ films with excellent superconductivity. As $x = 0.13, y = 0.76$, the maximum of zero-resistivity temperature T_c^0 of film is over 17 K, the upper critical field $H_{c2}(0) \approx 159.5$ T, and the critical current density J_c is higher than 10^6 A/cm² at 4 K. Moreover, the STEM images reveal that the interface region of $\text{Fe}_y\text{Se}_{1-x}\text{Te}_x/\text{TiO}_2/\text{SrTiO}_3$ heterostructure is sharp and clear, and no obvious atomic diffusion and migration was detected.

Results and discussion

In the published papers [14, 20-22], authors usually defined the nominal composition of the targets as the real composition for $\text{Fe}_y\text{Se}_{1-x}\text{Te}_x$ films. However, the deviation between the nominal composition and the real composition may affect the study on the mechanism of superconductivity for $\text{Fe}_y\text{Se}_{1-x}\text{Te}_x$ films. We determined the real composition of films by EDX mapping in SEM technology. Our experimental results show that there is a significant deviation between the nominal composition and the real composition in the two groups, as shown in tables 1 and 2. At the first, we fixed the content of Fe and adjusted the amount of Te doping in the targets (nominal composition in table 1). EDX results show that Te doping can have an impact not only on Se/Te ratio but also the Fe content in films. The optimal chemical composition may play an important role in films with excellent superconducting property. Base on this result, we measured the superconducting properties of these films and gave them in the following text. To explore the effect of Fe content on the superconductivity of $\text{Fe}_y\text{Se}_{1-x}\text{Te}_x$ films, we fixed the Se/Te ratio and change the Fe doping in the nominal composition, as shown in Table 2. It can be seen that the change of Fe doping in the nominal composition also leads to the change of the Fe content in the real composition,

but has little influence on the ratio of Se/Te. During the deposition, the transfer and growth rate of Fe/Se/Te elements are different, which may lead to the obvious deviation of chemical composition between target and film. Therefore, we think that it is inaccurate to directly define the nominal composition of the targets as the real composition of the films.

The XRD patterns of $\text{Fe}_y\text{Se}_{1-x}\text{Te}_x$ films are shown in Fig. 1. From Fig. 1, only $\text{Fe}_y\text{Se}_{1-x}\text{Te}_x$ and TiO_2 peaks are observed along the c -axis ($00l$), which indicates the $\text{Fe}_y\text{Se}_{1-x}\text{Te}_x$ epitaxial films to be single tetragonal phase. Our previous work confirmed that TiO_2 as a buffer layer could increase the lattice match between Fe(Se, Te) film and STO substrate, so as to enhance the superconducting property of Fe(Se, Te) film [23]. We find that with increasing Te doping, the ($00l$) peaks significantly shift to a low angle. The c -axis lattice parameters for $\text{Fe}_y\text{Se}_{1-x}\text{Te}_x$ films were obtained by fitting the (001) peak, as listed in table 1. The ionic radius of Te (Te^{2-} , 221 pm) is larger than that of Se (Se^{2-} , 198 pm) [24]. Te doping can increase the distance between the Fe plane and Se (Te) atom ($h_{\text{Fe-Se/Te}}$), which result in the increase of c -axis lattice parameters. Zhuang *et al* [25] and Ima *et al* [26] have reported the effect of chemical composition on the structure in $\text{FeSe}_{1-x}\text{Te}_x$ films. In our results, the increase of Te doping in targets can also raise the Fe content in the $\text{Fe}_y\text{Se}_{1-x}\text{Te}_x$ films. For $y > 1$ in table 1, we assume that the additional Fe may be incorporated in the inter-layer of Fe-Se/Te space. Thus, Fe content play a part in the change of lattice parameter. Shi. *et al* [22] assumed that two key factors affected the lattice parameters of thin films under the Fe-deficient conditions. The ionic radius of Fe is smaller than that of Se and Te. Fe vacancy phase leads to a smaller c -axis lattice parameter, while Se/Te interstitial phase leads to a larger c -axis in comparison with the stoichiometric phase. For table 2, with increasing the Fe doping, the c -axis lattice parameter of films increases. The above results show that the superconducting structures of $\text{Fe}_y\text{Se}_{1-x}\text{Te}_x$ films are not changed with $0.63 < y < 1.43$, whereas Te and Fe doping jointly influence the c -axis lattice parameter.

Figure 2 (a) shows the temperature dependence of the normalized resistivity $\rho/\rho_{300\text{K}}$ (ρ -T) for the $\text{Fe}_y\text{Se}_{1-x}\text{Te}_x$ films. For $0.03 \leq x \leq 0.23$ in Fig. 2 (a), as the temperature above the superconducting transition, the films only display metallic

behavior. However, for $x > 0.23$, the resistivity of films changes from semiconducting to metallic before superconducting transition. This change may attribute to the structure phase transition and magnetic phase transition that caused by Te doping. If we define the point of intersection of the two lines as the normal-state resistivity ρ_n , as shown in the inset of Fig. 2 (a), the onset transition temperature T_c^{onset} and zero-resistivity temperature T_c^0 are obtained from these ρ - T curves where the resistivity is 90% and 1% of the normal state resistivity ρ_n , respectively. The values of T_c^{onset} and T_c^0 for these samples were listed in table 1 and plotted in the 3D phase diagram, as shown in Fig. 2 (c). With increasing the Te doping, the T_c rises at first and then decreases. From Fig. 2 (c), the $\text{Fe}_{0.76}\text{Se}_{0.87}\text{Te}_{0.13}$ film exhibits the higher T_c^{onset} and T_c^0 about 18.95 K and 17.34 K, respectively. Surprising us, the composition of the $\text{Fe}_{0.76}\text{Se}_{0.87}\text{Te}_{0.13}$ film is not consistent with that of the single crystal, where the highest T_c is considered $x \approx 0.6$ in $\text{Fe}(\text{Se}_{1-x}\text{Te}_x)_{0.82}$ polycrystal sample, and located at the phase separation region of $0.1 \leq x \leq 0.3$ [12]. They argued that the single-phase of $\text{Fe}(\text{Se}_{1-x}\text{Te}_x)_{0.82}$ single crystals with the region of $0.1 \leq x \leq 0.3$ were not easy to obtained. However, Imai reported that the single-phase epitaxial films of $\text{FeSe}_{1-x}\text{Te}_x$ with $0.1 \leq x \leq 0.4$ could be successfully prepared on CaF_2 substrates, attributing to the strain effect between film and substrate [14]. Due to the different substrates, there is a difference in the suppression of phase separation and giant enhancement of T_c for $\text{Fe}_y\text{Se}_{1-x}\text{Te}_x$ films. Our experimental results display that the sudden suppression of T_c is observed at $0.03 \leq x < 0.13$, whereas T_c increases with decreasing x for $0.13 \leq x < 0.56$. The superconducting property is related to the Te and Fe content in $\text{Fe}_y\text{Se}_{1-x}\text{Te}_x$ film. Therefore, we must consider the effects of Fe vacancies on the superconductivity of $\text{Fe}_y\text{Se}_{1-x}\text{Te}_x$ films.

Figure 2 (b) shows the temperature dependence of the normalized resistivity $\rho/\rho_{300\text{K}}$ (ρ - T) near the optimal composition $\text{Fe}_y\text{Se}_{1-x}\text{Te}_x$ films, where $x \sim 0.15$ and $y \sim 0.76$. The results demonstrate the effects of Fe vacancies on the superconductivity of $\text{Fe}_y\text{Se}_{1-x}\text{Te}_x$ films. The T_c^{onset} and T_c^0 were listed in table 2 and plotted in the 3D phase diagram of Fig. 2 (b). Although we do not know the reason why the T_c^{onset} and T_c^0 increase with decreasing the Fe content near $y = 0.76$, the transition width broadens much more. This result further confirms that the optimal range is $x = 0.13 - 0.15$ and y

= 0.73 – 0.78 for the $\text{Fe}_y\text{Se}_{1-x}\text{Te}_x$ films.

Figure 2 (c) is a new 3D phase diagram for the $\text{Fe}_y\text{Se}_{1-x}\text{Te}_x$ films. The 3D phase diagram can be divided into three regions, which are superconductivity (SC), flux flow (FF), and normal state (NS), respectively. The 3D phase diagram demonstrates that the phase separation is absent, and that the optimal composition for the $\text{Fe}_y\text{Se}_{1-x}\text{Te}_x$ film on STO substrate is not $x \approx 0.5$ and $y = 1$ but $x \sim 0.13$ and $y \sim 0.76$. It should be noted that the dependence of T_c on x suddenly changes at the boundary defined by $0.03 \leq x < 0.13$ in our experiment. Thus, not only the decrease of T_c with $x \geq 0.13$ can be explained by the empirical law that shows the relation between T_c and structural parameters, but also the sudden suppression of T_c in films with $0.03 \leq x < 0.13$ can be explained by the orthorhombic distortion results in a suppression of T_c . As reported by Imai Y *et al.* [9], the orthorhombic distortion is applicable to the behavior of films, if a large orthorhombic distortion is observed only in films with $0 < x < 0.1$, which is consistent with our result of $0.03 \leq x < 0.13$. Chen *et al.* [27] and Bendele *et al* [28] pointed out that a few Fe vacancies are beneficial to improve the superconductivity and raise the superconducting transition temperature for $\text{Fe}_y\text{Se}_{1-x}\text{Te}_x$ films. The inhomogeneous distribution of Fe vacancies can induce the Fe disorder effect in the films with the $y < 1$. The first-principles calculation also showed that the Fe vacancies could effectively increase the number of electron carriers and change the electronic properties in the samples [22]. Therefore, in this experiment, the highest T_c^{onset} and T_c^0 occurred near $y = 0.76$. When the Te and Fe content exceed the optimal composition, the T_c^{onset} and T_c^0 of $\text{Fe}_y\text{Se}_{1-x}\text{Te}_x$ films decrease. For example, as $x = 0.56$, $y = 1.43$, the ρ does not down to 1% ρ_n , so the $\text{Fe}_{1.43}\text{Se}_{0.44}\text{Te}_{0.56}$ sample only has the T_c^{onset} about 8.03 K.

To understand the new phase diagram, we have measured the electrical transport and magnetization properties for the $\text{Fe}_y\text{Se}_{1-x}\text{Te}_x$ films in magnetic field. Here, we choose some typical results in the next part. Figure 3 (a) and (b) present the temperature dependence of resistivity of $\text{Fe}_{0.76}\text{Se}_{0.87}\text{Te}_{0.13}$ film in various magnetic fields up to 9 T applied perpendicular and parallel to the c -axis. With increasing the applied magnetic field, the resistive transition was broadened. At the same field, the width of superconducting transition ΔT_c for $H//c$ is larger than that for $H//ab$. This result

indicates that the $\text{Fe}_y\text{Se}_{1-x}\text{Te}_x$ films are anisotropic near T_c .

If we define the onset transition temperature T_c^{onset} as the critical temperature T_c , namely the field is the upper critical field H_{c2} , we can get the temperature of the upper critical field near T_c . The H - T phase diagram for $\text{Fe}_{0.72}\text{Se}_{0.94}\text{Te}_{0.06}$, $\text{Fe}_{0.76}\text{Se}_{0.87}\text{Te}_{0.13}$ and $\text{Fe}_{0.91}\text{Se}_{0.77}\text{Te}_{0.23}$ films is shown in Fig. 4. Using the Werthamer-Helfand-Hohenberg (WHH) formula [29] $H_{c2} = -0.69T_c[dH_{c2}/dT]_{T_c}$, the upper critical field $H_{c2}(0)$ of $\text{Fe}_{0.72}\text{Se}_{0.94}\text{Te}_{0.06}$, $\text{Fe}_{0.76}\text{Se}_{0.87}\text{Te}_{0.13}$ and $\text{Fe}_{0.91}\text{Se}_{0.77}\text{Te}_{0.23}$ films were estimated about 109.6 T, 159.5 T and 134.2 T, respectively. It implies that the values of upper critical field $H_{c2}(0)$ also depend on the chemical composition of $\text{Fe}_y\text{Se}_{1-x}\text{Te}_x$ films. From Fig. 4, The anisotropic factor γ can be obtained according to the formula: $\gamma = [dH_{c2}^{ab}(T)/dT] / [dH_{c2}^c(T)/dT]$ near T_c . The γ value of $\text{Fe}_{0.72}\text{Se}_{0.94}\text{Te}_{0.06}$, $\text{Fe}_{0.76}\text{Se}_{0.87}\text{Te}_{0.13}$ and $\text{Fe}_{0.91}\text{Se}_{0.77}\text{Te}_{0.23}$ films are 2.59, 2.09, and 1.72, respectively. The increase of Te doping inhibits the anisotropic and enhances the isotropy in $\text{Fe}_y\text{Se}_{1-x}\text{Te}_x$ films. Te doping may enhance the correlation between Fe-Se/Te layers, which is conducive to the transmission of electrons along the c -axis direction and result in the decrease in anisotropy.

The effective pinning energy is an important parameter to enhance the capacity of carrying current for superconducting materials. According to the thermally activated flux flow (TAFF) theory, the $\ln\rho - 1/T$ in the TAFF region can be described using an Arrhenius relation [30-32], $\rho = \rho_0 \exp(-\frac{U_0}{K_B T})$ where U_0 is the effective pinning energy. Figure 5 (a) and (b) shows the linear relationship between $\ln\rho$ and $1/T$ of the $\text{Fe}_{0.76}\text{Se}_{0.87}\text{Te}_{0.13}$ film. From the absolute slope of $\ln\rho - 1/T$ curves, we can obtain the effective pinning energy U_0 of $\text{Fe}_{0.72}\text{Se}_{0.94}\text{Te}_{0.06}$, $\text{Fe}_{0.76}\text{Se}_{0.87}\text{Te}_{0.13}$ and $\text{Fe}_{0.91}\text{Se}_{0.77}\text{Te}_{0.23}$ films, respectively, as shown in Fig. 5 (c). It can be found that the U_0 value of $\text{Fe}_{0.76}\text{Se}_{0.87}\text{Te}_{0.13}$ is larger than that of $\text{Fe}_{0.72}\text{Se}_{0.94}\text{Te}_{0.06}$ and/or $\text{Fe}_{0.91}\text{Se}_{0.77}\text{Te}_{0.23}$ in the same field. Furthermore, U_0 values for $H//ab$ plane are much higher than that for $H//c$ plane, indicating the flux pinning is anisotropic, and the magnetic field dependence of U_0 follows a power law U_0 (K) $\sim H^{-\alpha}$. The parameter α of three samples is close for

$H//ab$. However, there is an obvious crossover that occurred at $H \approx 2$ T for $H//c$. The parameter α for $H//c$ is close to 0.15 in the low field and 0.5 in the high field. Generally, the parameter α is related to the pinning mechanism of superconductors [33]. The core pinning is responsible for $\alpha = 3/2$, while the linear pinning is responsible for $\alpha = 1$. As $\alpha = 1/2$, the pinning mechanism in superconductor is generally considered as the planar pinning [34]. It is possible that the flux pinning in $\text{Fe}_y\text{Se}_{1-x}\text{Te}_x$ films is the collective flux pinning, including planar pinning and 3 D volume cores pinning.

The critical current density J_c is also an important parameter for high quality epitaxial superconducting films. To study the effect of chemical composition on the critical current density of $\text{Fe}_y\text{Se}_{1-x}\text{Te}_x$ films, we have measured the magnetization hysteresis loops in fields parallel to the c -axis from 0 to ± 9 T. Figure 6 shows the M - H loops of $\text{Fe}_{0.91}\text{Se}_{0.77}\text{Te}_{0.23}$ film at various temperatures. The M - H loops show symmetric field dependence. As the field increases, the magnetization of film decreases.

The critical current density J_c was estimated from the M - H loops by the Bean critical state model [35]: $J_c = 20 \frac{\Delta M}{a(1-a/3b)}$. Where $\Delta M = M(+)-M(-)$, $M(+)$ and $M(-)$ are the magnetizations when sweeping fields up and down, respectively. a and b ($a < b$) are the $\text{Fe}_y\text{Se}_{1-x}\text{Te}_x$ film's cross-sectional dimension. The field dependence of the critical current density J_c at various temperatures is shown in Fig. 7. At a constant temperature, the magnetic field H dependence of critical current density J_c follows a semi-exponent-law behavior: $J_c \propto H^{-\delta}$. Where δ is a parameter, meaning the decreasing rate of J_c with the field H increasing. We can see that the J_c decreases with the field H increasing. The calculated J_c at 4 K and 0 T for $\text{Fe}_{0.72}\text{Se}_{0.94}\text{Te}_{0.06}$, $\text{Fe}_{0.76}\text{Se}_{0.87}\text{Te}_{0.13}$, $\text{Fe}_{0.91}\text{Se}_{0.77}\text{Te}_{0.23}$ films are about 4.46×10^5 A/cm², 4.51×10^6 A/cm² and 4.05×10^6 A/cm², respectively. Compared with the three samples, it also confirms that the optimal composition is beneficial for $\text{Fe}_y\text{Se}_{1-x}\text{Te}_x$ films exhibiting excellent superconductivity.

The interface structure plays a vital role in determining the superconducting properties for $\text{Fe}_y\text{Se}_{1-x}\text{Te}_x$ films. Using the STEM analysis, we could reveal the

$\text{Fe}_{0.76}\text{Se}_{0.87}\text{Te}_{0.13}/\text{TiO}_2/\text{STO}$ microstructure and determined the morphology of the interface. The thicknesses of $\text{Fe}_{0.76}\text{Se}_{0.87}\text{Te}_{0.13}$ and TiO_2 film are about 32.4 nm and 29.5 nm, respectively. Figure 8 (a) shows the overview image of the $\text{Fe}_{0.76}\text{Se}_{0.87}\text{Te}_{0.13}/\text{TiO}_2/\text{STO}$ interface. It can be seen that the heterostructure interface is sharp and clean without large-scale defects. The TiO_2 buffer was successfully deposited between the $\text{Fe}_{0.76}\text{Se}_{0.87}\text{Te}_{0.13}$ film and STO substrate. Figure 8 (b) shows the high-magnification HAADF image of $\text{Fe}_{0.76}\text{Se}_{0.87}\text{Te}_{0.13}/\text{TiO}_2$. The Fe, Se/Te, Ti and O atoms are arranged neatly at the interface. In this case, the $\text{Fe}_{0.76}\text{Se}_{0.87}\text{Te}_{0.13}$ structure with a tetragonal space group $P4/nmm$ is very simple, and each unit cell contains 3 quintuple layers (QLs), which are bonded by van der Waals (vdW) [9]. The TiO_2 unit cell has two Ti-O triple layers, which grow on STO along the $(00l)$ direction. From Fig. 8 (b), a nanoscale damaged layer (or transition layer) was formed between the TiO_2 and $\text{Fe}_{0.76}\text{Se}_{0.87}\text{Te}_{0.13}$ interface. To determine the formation of this transition layer, the Atomic resolution EDX mapping was conducted in this area. The chemical elemental maps of Fig. 8 (c) confirm the suggestion from HAADF imaging that the atoms are arranged regularly without obvious diffusion and migration. Such high quality heterostructure had a significant influence on the enhancement of superconductivity for $\text{Fe}_y\text{Se}_{1-x}\text{Te}_x$ films.

Conclusion

In summary, we successfully prepared the $\text{Fe}_y\text{Se}_{1-x}\text{Te}_x$ thin films with $0.03 \leq x \leq 0.56$ and $0.63 \leq y \leq 1.43$ by PLD. Our experimental results confirmed the significant deviation between the nominal compositions of targets and the real compositions of $\text{Fe}_y\text{Se}_{1-x}\text{Te}_x$ films. Chemical composition does affect the superconducting properties such as J_c and H_{c2} in $\text{Fe}_y\text{Se}_{1-x}\text{Te}_x$ films. A new 3D phase diagram is presented from the experimental results of electrical transport, which reveals that the optimal composition for $\text{Fe}_y\text{Se}_{1-x}\text{Te}_x$ films is $x = 0.13 - 0.15$ and $y = 0.73 - 0.78$. The field dependence of flux pinning energy displayed that the increase of Te doping can enhance the flux pinning in the $\text{Fe}_y\text{Se}_{1-x}\text{Te}_x$ films. STEM investigation shows that the $\text{Fe}_{0.76}\text{Se}_{0.87}\text{Te}_{0.13}/\text{TiO}_2/\text{STO}$ heterostructure has a sharp interface and exhibits almost no atomics intermixing. Our study results provide some further understanding on the

mechanism of superconducting properties for $\text{Fe}_y\text{Se}_{1-x}\text{Te}_x$ films, which has a certain guiding significance and reference value for the potential application of iron-based superconductors.

Methods

The PLD targets were prepared by the self-flux method with high purity materials (Fe 99.99%, Te 99.999% and Se 99.999%) in the stoichiometric proportion. Fe, Se and Te were fully ground and squeezed into a 3/4 inch block, and then encapsulated in a vacuum quartz tube. The vacuum quartz tube was calcined in a muffle furnace at 850 °C for 72 hours, then slowly cooled down to room temperature with the rate of 3 °C/min. The $\text{Fe}_y\text{Se}_{1-x}\text{Te}_x$ epitaxial films were deposited on STO single crystalline substrates at 300 °C by PLD in a high vacuum ($\sim 10^{-7}$ mbar). The distance between target and substrate was set at ~ 70 mm. A KrF excimer laser (248nm) was used for deposition with an energy density of 2.0 J/cm² and a repetition frequency of 2 Hz. The size of the STO substrate is 5 mm × 5 mm. TiO₂ film as a buffer layer was firstly deposited on STO substrate by PLD to improve the lattice matching between $\text{Fe}_y\text{Se}_{1-x}\text{Te}_x$ film and STO substrate. The deposition temperature and deposition time for $\text{Fe}_y\text{Se}_{1-x}\text{Te}_x$ and TiO₂ film were 300 °C and 15 min, 600 °C and 4.5 min, respectively. After deposition, the films were annealed to room temperature at the rate of 5 °C/min.

X-ray diffraction (XRD) patterns using the $\theta/2\theta$ method were measured by Bruker D8 with $\text{CuK}\alpha$ radiation ($\lambda = 1.54 \text{ \AA}$). The chemical composition of $\text{Fe}_y\text{Se}_{1-x}\text{Te}_x$ films was determined by energy dispersive x-ray spectroscopy (EDX) in a Gemini 500 scanning electron microscope (SEM) mapping. The measurements of electrical transport were carried out via the physical property measurement system (PPMS-9 T, Quantum Design). Magnetization measurements on films with 100 Oe/s of sweep rate were performed in vibrating sample magnetometer (VSM). The microstructures of $\text{Fe}_y\text{Se}_{1-x}\text{Te}_x$ films were examined by scanning transmission electron microscopy (STEM, FEI Titan G2 60-300 aberration). Samples for the STEM were cut and milled in a focused ion beam (FIB, FEI Helios Nanolab 600) according to the so-called micro-bridge sampling technique.

Acknowledgements

The authors are grateful for the financial support of the Ministry of Science and Technology of China (2017YFA0303200), the National Natural Science Foundation of China (11671203), and the National Key Research and Development Program of China (2016YFA0300401).

Author Contributions

Yalin Zhang, Tong Wang, Zhihe Wang and Zhongwen Xing conceived the experiments; Yalin Zhang conducted the experiments; Yalin Zhang, Zhihe Wang, and Zhongwen Xing analysed the results; Yalin Zhang and Zhihe Wang wrote the paper. All authors have reviewed the manuscript.

Declaration of competing interest

The authors declare no competing financial interests.

Reference

- [1] Kamihara, Y. *et al.* Iron-based layered superconductor $\text{La}[\text{O}_{1-x}\text{F}_x]\text{FeAs}$ ($x = 0.05 - 0.12$) with $T_c = 26$ K. *J. Am. Chem. Soc.* **130**, 3296 (2008).
- [2] Hsu, F. C. *et al.* Superconductivity in the PbO-type structure α -FeSe. *P. Natl. Acad. Sci. USA* **105**, 14262 (2008).
- [3] Medvedev, S. *et al.* Electronic and magnetic phase diagram of β - $\text{Fe}_{1.01}\text{Se}$ with superconductivity at 36.7 K under pressure. *Nat. Mater.* **8**, 630 (2009).
- [4] Margadonna, S. *et al.* Pressure evolution of the low-temperature crystal structure and bonding of the superconductor FeSe ($T_c = 37$ K). *Phys. Rev. B* **80**, 064506 (2009).
- [5] Ge, J. F. *et al.* Superconductivity above 100 K in single-layer FeSe films on doped SrTiO_3 . *Nat. Mater.* **14**, 285 (2015).
- [6] Hanzawa, K. *et al.* Electric field-induced superconducting transition of insulating FeSe thin film at 35 K. *Proc. Natl. Acad. Sci. USA* **113**, 3986 (2016).
- [7] Zhang, H. *et al.* Origin of charge transfer and enhanced electron-phonon coupling in single unit-cell FeSe films on SrTiO_3 . *Nat. Commun.* **8**, 1 (2017).
- [8] Zhou, G. Y. *et al.* Interface enhanced superconductivity in monolayer FeSe films on MgO (001): charge transfer with atomic substitution. *Sci. Bull.* **63**, 747 (2018).
- [9] Sims, H. *et al.* Intrinsic interfacial van der Waals monolayers and their effect on the high-temperature superconductor FeSe/ SrTiO_3 . *Phys. Rev. B* **100**, 144103 (2019).
- [10] Li, F. S. *et al.* Atomically resolved FeSe/ SrTiO_3 (001) interface structure by scanning transmission electron microscopy. *2D Mater.* **3**, 024002 (2016).
- [11] Yeh, K. W. *et al.* Tellurium substitution effect on superconductivity of the α -phase iron selenide. *Europhys Lett.* **84**, 37002 (2008).
- [12] Fang, M. H. *et al.* Superconductivity close to magnetic instability in $\text{Fe}(\text{Se}_{1-x}\text{Te}_x)_{0.82}$. *Phys. Rev. B* **78**, 224503 (2008).
- [13] Liu, T. J. *et al.* From $(\pi, 0)$ magnetic order to superconductivity with (π, π) magnetic resonance in $\text{Fe}_{1.02}\text{Te}_{1-x}\text{Se}_x$. *Nat. Mater.* **9**, 718 (2010).
- [14] Imai, Y. *et al.* Suppression of phase separation and giant enhancement of superconducting transition temperature in $\text{FeSe}_{1-x}\text{Te}_x$ thin films. *Proc. Natl. Acad. Sci. USA* **112**, 1937 (2015).

- [15] Bellingeri, E. *et al.* $T_c = 21$ K in epitaxial $\text{FeSe}_{0.5}\text{Te}_{0.5}$ thin films with biaxial compressive strain. *Appl. Phys. Lett.* **96**, 102512 (2010).
- [16] Huang, S. X. *et al.* Control of tetrahedral coordination and superconductivity in $\text{FeSe}_{0.5}\text{Te}_{0.5}$ thin films. *Phys. Rev. Lett.* **104**, 217002 (2010).
- [17] Iida, K. *et al.* Generic Fe buffer layers for Fe-based superconductors: Epitaxial $\text{FeSe}_{1-x}\text{Te}_x$ thin films. *Appl. Phys. Lett.* **99**, 202503 (2011).
- [18] Bellingeri, E. *et al.* Tuning of the superconducting properties of $\text{FeSe}_{0.5}\text{Te}_{0.5}$ thin films through the substrate effect. *Supercond. Sci. Technol.* **25**, 084022 (2012).
- [19] Iida, K. *et al.* Intrinsic pinning and the critical current scaling of clean epitaxial Fe (Se, Te) thin films. *Phys. Rev. B* **87**, 104510 (2013).
- [20] Ichinose, A. *et al.* Microscopic analysis of the chemical reaction between Fe(Te, Se) thin films and underlying CaF_2 . *Supercond. Sci. Technol.* **26**, 075002 (2013).
- [21] Zhuang, J. C. *et al.* Pauli-limited effect in the magnetic phase diagram of $\text{FeSe}_x\text{Te}_{1-x}$ thin films. *Appl. Phys. Lett.* **107**, 222601 (2015).
- [22] Zhuang, J. C. *et al.* Enhancement of transition temperature in $\text{Fe}_x\text{Se}_{0.5}\text{Te}_{0.5}$ film via iron vacancies. *Appl. Phys. Lett.* **104**, 262601 (2014).
- [23] Huang, J. F. *et al.* Linear correlation between the c-axis lattice constant and superconducting critical temperature in $\text{FeSe}_{0.5}\text{Te}_{0.5}$ thin films. *Mater. Res. Express* **7**, 046002 (2020).
- [24] Wu, Z. F. *et al.* Anisotropic flux pinning energy in $\text{FeSe}_x\text{Te}_{1-x}$ single crystals. *Physica. C* **528**, 39 (2016).
- [25] Zhuang, J. C. *et al.* Pauli-limited effect in the magnetic phase diagram of $\text{FeSe}_x\text{Te}_{1-x}$ thin films. *Sci. Rep.* **4**, 1 (2014).
- [26] Imai, Y. *et al.* Control of structural transition in $\text{FeSe}_{1-x}\text{Te}_x$ thin films by changing substrate materials. *Sci. Rep.* **7**, 1 (2017).
- [27] Chen, T. K. *et al.* Fe-vacancy order and superconductivity in tetragonal $\beta\text{-Fe}_{1-x}\text{Se}$. *Proc. Natl. Acad. Sci. USA* **111**, 63 (2014).
- [28] Bendele, M. *et al.* Tuning the superconducting and magnetic properties of $\text{Fe}_y\text{Se}_{0.25}\text{Te}_{0.75}$ by varying the iron content. *Phys. Rev. B* **82**, 212504 (2010).
- [29] Werthamer, N. R. *et al.* Temperature and purity dependence of the superconducting critical field, H_{c2} . III. Electron spin and spin-orbit effects. *Phys. Rev.* **147**, 295 (1966).

- [30] Palstra, T. T. M. *et al.* Thermally activated dissipation in $\text{Bi}_{2.2}\text{Sr}_2\text{Ca}_{0.8}\text{Cu}_2\text{O}_{8+\delta}$. *Phys. Rev. Lett.* **61**, 1662 (1988).
- [31] Palstra, T. T. M. *et al.* Dissipative flux motion in high-temperature superconductors. *Phys. Rev. B* **41**, 6621 (1990).
- [32] Xing, X. Z. *et al.* Thermally activated flux flow, vortex-glass phase transition and the mixed-state Hall effect in 112-type iron pnictide superconductors. *Sci. China Phys. Mec.* **61**, 127406 (2018)
- [33] Kucera, J. T. *et al.* Magnetic-field and temperature dependence of the thermally activated dissipation in thin films of $\text{Bi}_2\text{Sr}_2\text{CaCu}_2\text{O}_{8+\delta}$. *Phys. Rev. B* **46**, 11004 (1992).
- [34] Mao, R. *et al.* Effect of Te-doping on the superconducting characteristics of FeSe single crystal. *J. Alloy. Compd.* **809**, 151851 (2019).
- [35] Bean, C. P. Magnetization of high-field superconductors. *Rev. Mod. Phys.* **36**, 31 (1964).

Figure captions

Fig. 1. X-ray diffraction patterns of $\text{Fe}_y\text{Se}_{1-x}\text{Te}_x$ thin films.

Fig. 2. (a), (b) Temperature dependence of resistivity from 2 to 300 K for $\text{Fe}_y\text{Se}_{1-x}\text{Te}_x$ thin films. (a) $(x, y) = (0.03, 0.63), (0.06, 0.72), (0.13, 0.76), (0.23, 0.91), (0.34, 1.09)$ and $(0.56, 1.43)$. Inset: enlarged plot for the definition of normal-state resistivity ρ_n . (b) $(x, y) = (0.15, 0.73), (0.13, 0.76)$ and $(0.16, 0.78)$. Inset: the enlarged ρ - T curve near T_c . (c) Sketch of the proposed temperature doping 3D phase diagram for $\text{Fe}_y\text{Se}_{1-x}\text{Te}_x$ superconducting system, showing regions of superconductivity (SC), flux flow (FF) and normal state (NS).

Fig. 3. Temperature dependence of resistivity near T_c in various magnetic fields for $\text{Fe}_{0.76}\text{Se}_{0.87}\text{Te}_{0.13}$ thin film. (a) $H//c$ -axis and (b) $H//ab$ -axis.

Fig. 4. Upper critical field versus temperature phase diagram determined by $\rho/\rho_n = 90\%$. (a) $\text{Fe}_{0.72}\text{Se}_{0.94}\text{Te}_{0.06}$, (b) $\text{Fe}_{0.76}\text{Se}_{0.87}\text{Te}_{0.13}$, (c) $\text{Fe}_{0.91}\text{Se}_{0.77}\text{Te}_{0.23}$.

Fig. 5. $\ln\rho$ versus $1/T$ curves in various magnetic fields of $\text{Fe}_{0.76}\text{Se}_{0.87}\text{Te}_{0.13}$ thin film. (a) $H//c$ -axis; (b) $H//ab$ -axis. (c) Magnetic field dependence of the effective flux pinning energy for $\text{Fe}_{0.72}\text{Se}_{0.94}\text{Te}_{0.06}$, $\text{Fe}_{0.76}\text{Se}_{0.87}\text{Te}_{0.13}$ and $\text{Fe}_{0.91}\text{Se}_{0.77}\text{Te}_{0.23}$ thin films.

Fig. 6. Magnetic hysteresis loops of $\text{Fe}_{0.91}\text{Se}_{0.77}\text{Te}_{0.23}$ film at various temperatures in magnetic field parallel to the c -axis.

Fig. 7. Magnetic field dependence of critical current density J_c at various temperatures for $\text{Fe}_{0.72}\text{Se}_{0.94}\text{Te}_{0.06}$, $\text{Fe}_{0.76}\text{Se}_{0.87}\text{Te}_{0.13}$ and $\text{Fe}_{0.91}\text{Se}_{0.77}\text{Te}_{0.23}$ thin films.

Fig. 8. (a) Overview image of the $\text{Fe}_{0.76}\text{Se}_{0.87}\text{Te}_{0.13}/\text{TiO}_2/\text{STO}$ thin film interface. (b) Atomically resolved HADDF-STEM image of $\text{Fe}_{0.76}\text{Se}_{0.87}\text{Te}_{0.13}/\text{TiO}_2$ heterostructure. (c) EDX-mapping results shows the distribution of Fe (red), Se (green), Te (blue) Ti (magenta), O (cyan).

Table captions

Table 1. The composition, onset and zero-resistivity temperature, and c -axis lattice parameter of thin films for nominal composition $\text{FeSe}_{1-x}\text{Te}_x$ targets.

Table 2. The composition, onset and zero-resistivity temperature, and c -axis lattice parameter of thin films for nominal composition $\text{Fe}_y\text{Se}_{0.4}\text{Te}_{0.6}$ targets.

Figure 1

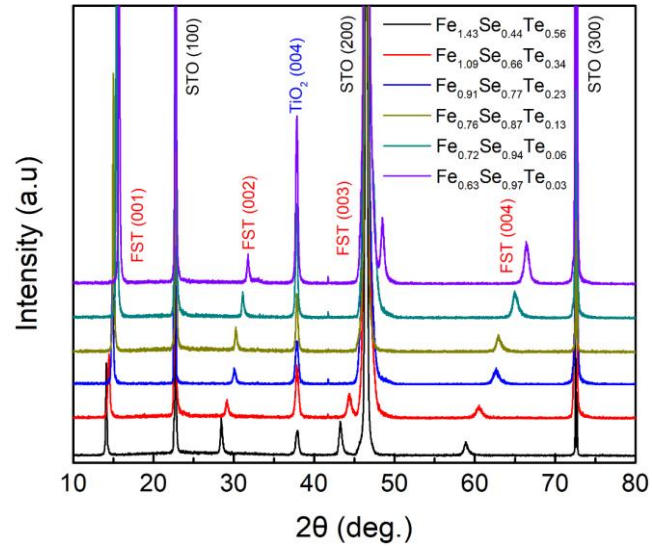


Figure 2

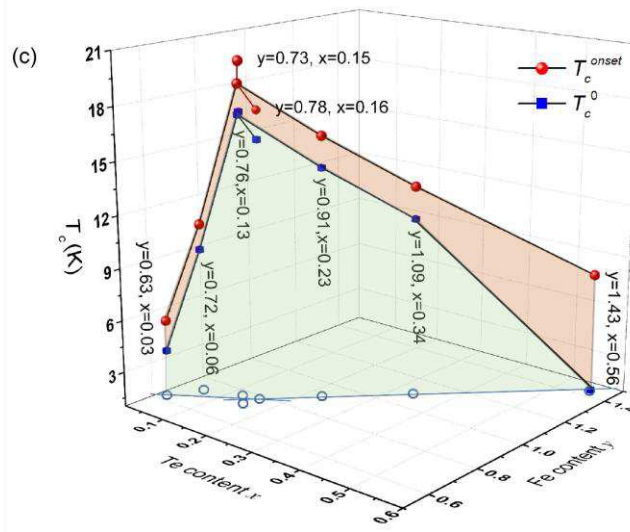
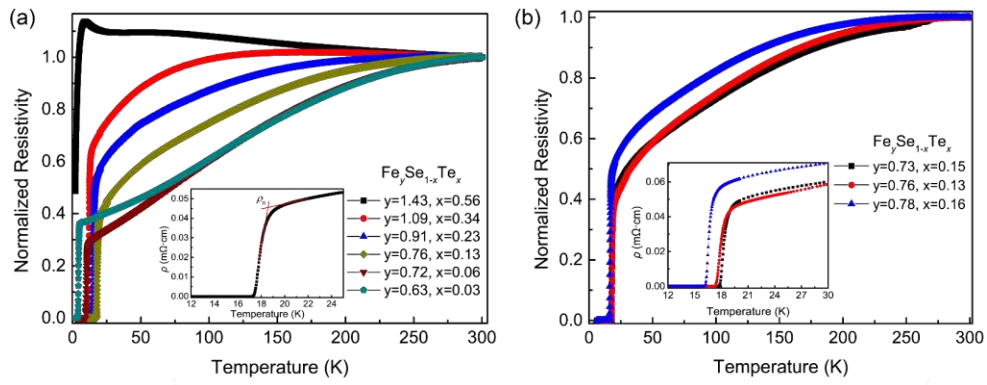


Figure 3

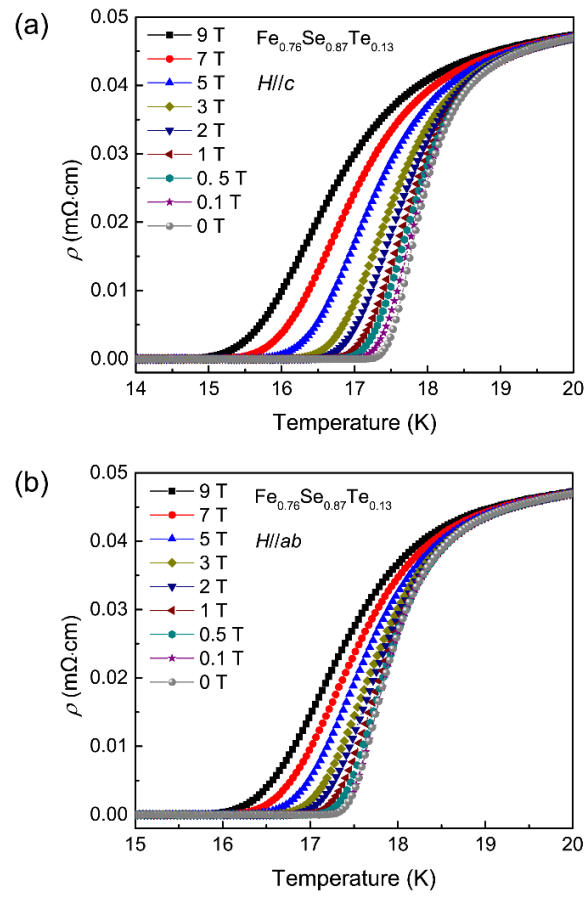


Figure 4

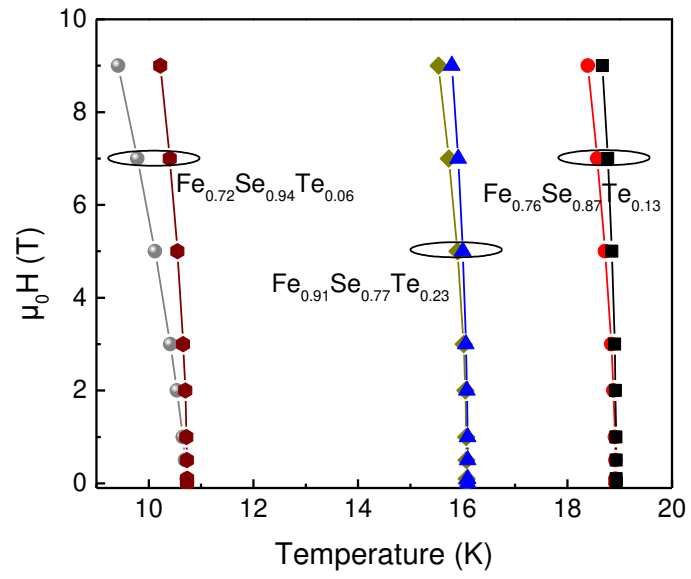


Figure 5

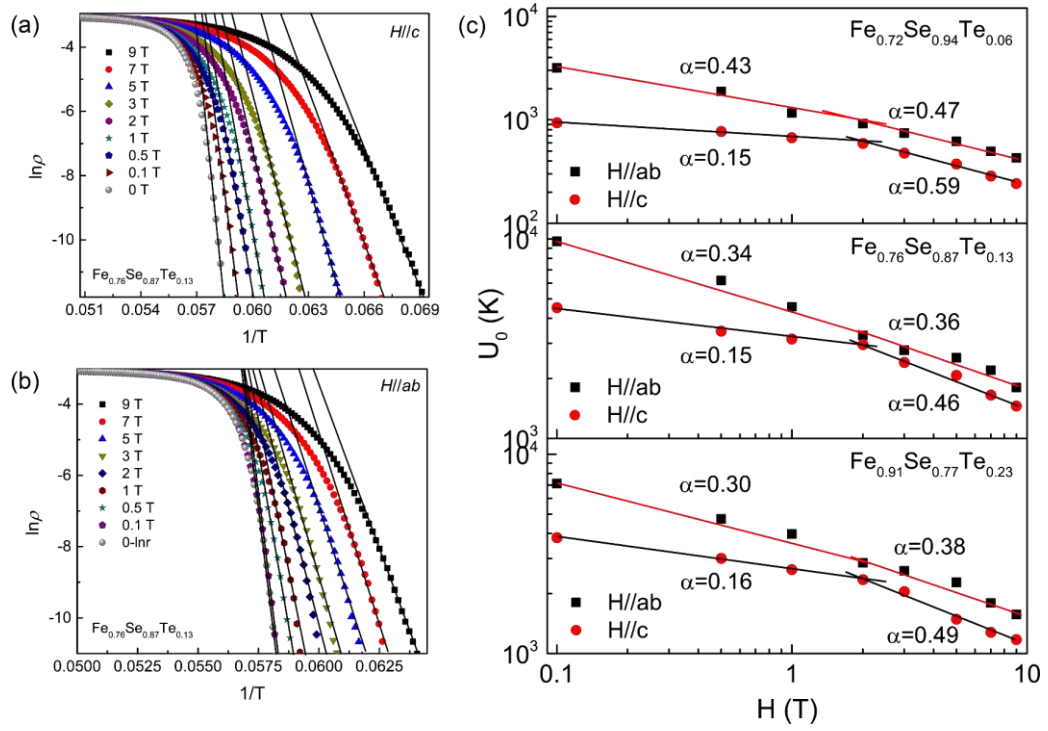


Figure 6

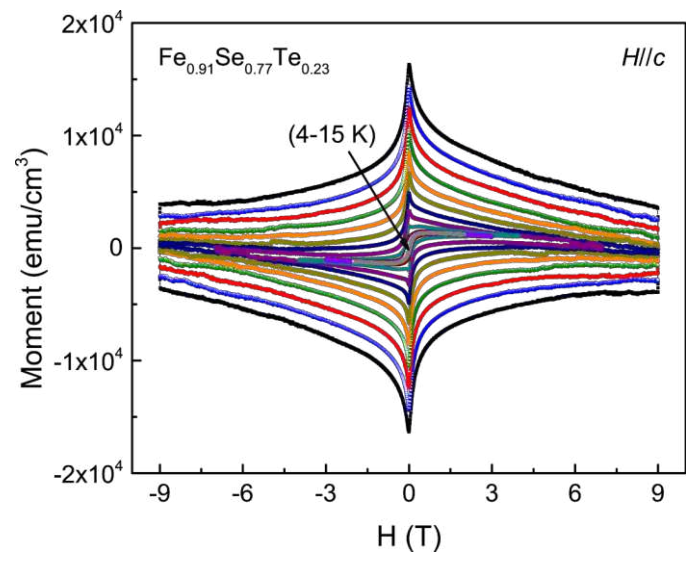


Figure 7

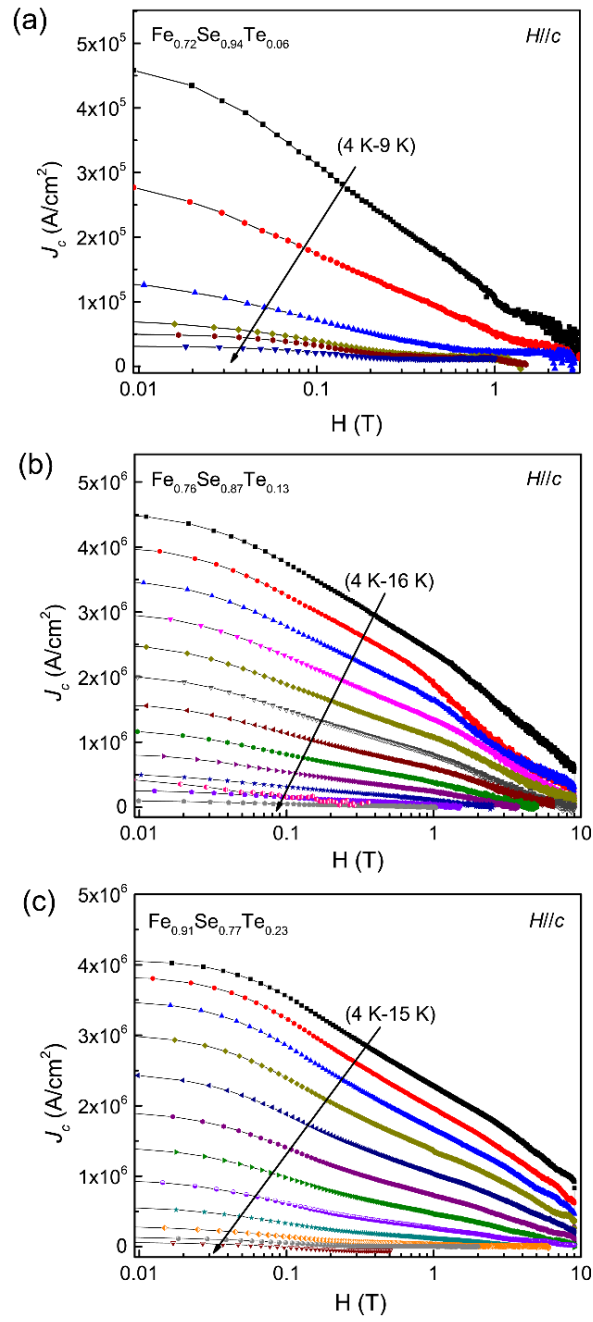


Figure 8

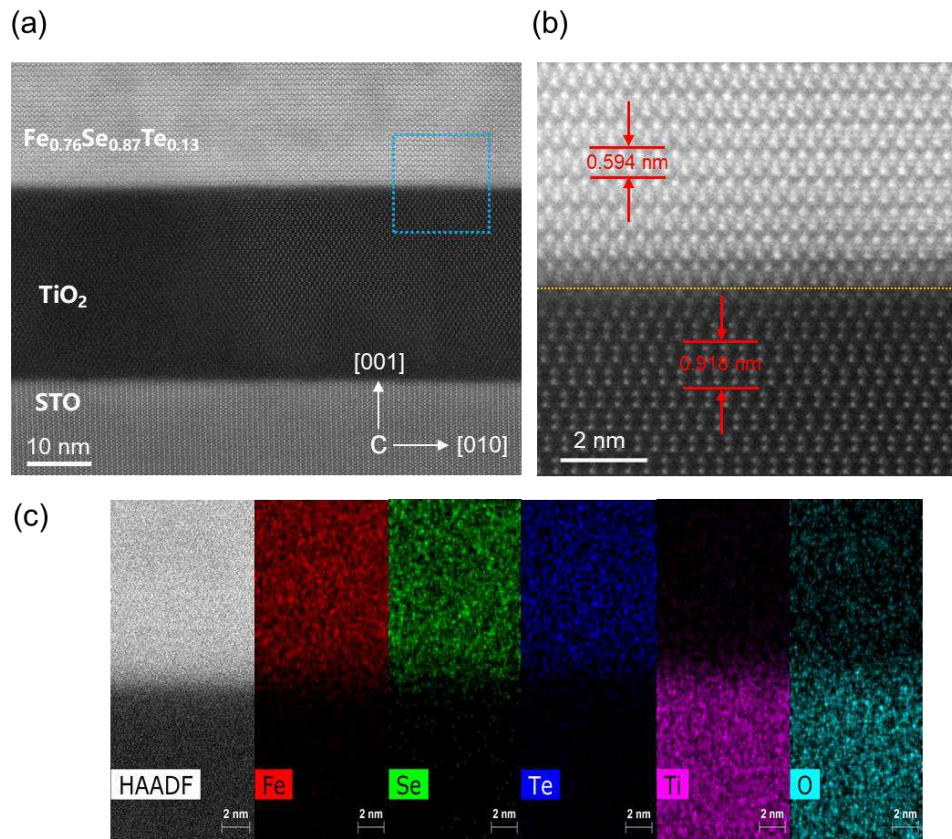


Table 1

nominal composition	real composition (± 0.02)	T_c^{onset} (K)	T_c^0 (K)	c parameter (\AA)
FeSe _{0.6} Te _{0.4}	Fe _{0.63} Se _{0.97} Te _{0.03}	5.49	3.71	5.6361
FeSe _{0.5} Te _{0.5}	Fe _{0.72} Se _{0.94} Te _{0.06}	10.73	9.44	5.7526
FeSe _{0.4} Te _{0.6}	Fe _{0.76} Se _{0.87} Te _{0.13}	18.95	17.34	5.8398
FeSe _{0.3} Te _{0.7}	Fe _{0.91} Se _{0.77} Te _{0.23}	16.13	14.35	5.9486
FeSe _{0.2} Te _{0.8}	Fe _{1.09} Se _{0.66} Te _{0.34}	13.21	11.37	6.0502
FeSe _{0.1} Te _{0.9}	Fe _{1.43} Se _{0.44} Te _{0.56}	8.03	-	6.1973

Table 2

nominal composition	real composition (± 0.02)	T_c^{onset} (K)	T_c^0 (K)	c parameter (\AA)
Fe _{0.9} Se _{0.4} Te _{0.6}	Fe _{0.73} Se _{0.85} Te _{0.15}	20.35	17.55	5.7287
FeSe _{0.4} Te _{0.6}	Fe _{0.76} Se _{0.87} Te _{0.13}	18.95	17.34	5.8398
Fe _{1.1} Se _{0.4} Te _{0.6}	Fe _{0.78} Se _{0.84} Te _{0.16}	17.64	16.01	6.0047